Research Article

Manal M. Alqarni, Rajwali Khan*, Wajdi Alghamdi, Mashael A. Aljohani, Taza Gul*, and Emad E. Mahmoud

A titanium oxide- and silver-based hybrid nanofluid flow between two Riga walls that converge and diverge through a machine-learning approach

https://doi.org/10.1515/ntrev-2025-0212
received March 19, 2025; accepted August 17, 2025

Abstract: The silver (Ag) and titanium oxide (TiO_2) nanoparticle combination is responsible for the uniform heat distribution, which enhances the heat transfer of the hybrid nanofluid (HNF). The HNFs are capable of enhancing heat transfer, which has significant applications in energy resources and heat exchangers. The flow is the result of the convergence and divergence of two non-parallel Riga walls. The control volume finite element method is employed to obtain a microscopic view of the HNFs between non-parallel rigid walls. Furthermore, the governing equations of the physical system are solved using a machine learning technique called wavelet-based physics-informed neural network. The methodology's implementation is flexible due to the nonlinearity of the equations, and the activation function used enhances the accuracy of the solution. Enhancement of the heat transfer rate is obtained by varying the embedded parameters. The percentage increase in heat transfer rate is achieved from 30.7 to 24.3% using the Ag and TiO_2 HNFs. The fuzzy inference technique function outputs, mean squared error results, and error normalized squared error are observed with the best validation employing the neural network. In the end, the results are compared with the existing literature.

Keywords: Riga walls, converge and diverge channel, Ag + TiO_2 nanomaterials, artificial neural network, control volume finite element method

1 Introduction

Small metal particles are dispersed in a base solvent to form a nanofluid. The base solvent comprised water, oil, blood, and other substances. Engineering, thermal exchangers, biomedicine, and the paint industry are the main applications of nanofluids. The thermal efficiency of base fluids is not usually suitable for enhancing the thermal performance of devices, so metal particles are added to improve their thermal capacity. Different nanoparticles have been utilized by Ahmed *et al.* [1] to enhance heat transfer. Numerical and statistical analyses have been used by them to predict the thermal enhancement. Thumma *et al.* [2] performed research on nanofluids that utilize convergent and divergent channels. Their study's outcome is centered around enhancing heat transfer. Khan *et al.* [3] used Cu and Al_2O_3 nanoparticles to analyze fluid flow and heat transfer, taking into account nonparallel walls. The medical applications of Fe_2O_3 nanoparticles, which utilize blood as their base fluid, were discussed by Rehman *et al.* [4]. The Fe_2O_3 nanoparticles were used as the drug delivery carrier, and their focus was on their medical advantages. However, the thermal performance and chemical performance of the nanoparticles are limited. By mixing different nanoparticles, the thermal efficiency of the nanofluid can be increased by avoiding the limitation of thermal conductivity (TC) of a single particle.

*** Corresponding author: Rajwali Khan,** National Water and Energy Center, United Arab Emirates University, Al ain, 15551, Abu Dhabi, United Arab Emirates, e-mail: rajwali@uaeu.ac.ae
*** Corresponding author: Taza Gul,** Department of Mathematics, City University of Science and Information Technology, Peshawar, 25000, Pakistan; DoST- Directorate General of Science & Technology, Khyber Pakhtunkhwa, Peshawar, 25000, Pakistan, e-mail: tazagul@cusit.edu.pk
Manal M. Alqarni: Department of Mathematics, College of Sciences, King Khalid University, Abha, 61413, Saudi Arabia
Wajdi Alghamdi: Department of Information Technology, Faculty of Computing and Information Technology, King Abdulaziz University, Jeddah, 80261, Saudi Arabia
Mashael A. Aljohani: Department of Mathematics and Statistics, College of Science in Yanbu, Taibah University, Madinah, Saudi Arabia
Emad E. Mahmoud: Department of Mathematics and Statistics, College of Science, Taif University, P.O. Box 11099, Taif, 21944, Saudi Arabia

It has been observed over time that mixing two different nanoparticles in a pure fluid can further improve its thermal flow characteristics. This new type of fluid is termed the hybrid nanofluid (HNF) [5]. The use of nanoparticles from other materials in an HNF flow is a sophisticated idea in fluid dynamics that alters the thermal and rheological characteristics of base fluids. The typical approach to distributing nanoparticles in a traditional fluid involves distributing two or more types of nanoparticles. In comparison to conventional single-component nanofluids, the synergy between various nanoparticles produces better thermal conductance, greater heat transfer rates, and increased stability, as noticed by Algehyne *et al.* [6]. The thermal efficiency of the base fluid can be improved by the thermal characteristics of HNFs, which are their advantages.

Kumar *et al.* [7] and Bompally *et al.* [8] used HNFs, which resulted in enhanced heat transfer and had numerous applications in the field of thermal engineering. The thermal flow of HNFs is the subject of extensive research because of their versatile applications and promising future in heat transfer systems. Khan *et al.* [3] used the idea of converging and diverging channels to enhance heat transfer effects by exploring the radiative flow of HNFs. Alnahdi *et al.* [9] predicted that a nanofluid with various nanoparticles would work as a drug delivery agent when subjected to a converging and a diverging channel. The HNF flow in terms of non-parallel plates resulted in thermal enhancement, which was explored by Li *et al.* [10]. Jabir *et al.* [11] examined the thermal observations for nanofluid and hybrid nanomaterials as they rotated on a bidirectional moving surface for medical applications.

Kolsi *et al.* [12] examined the polymer/carbon nanotube matrix nanocomposites across parallel sheets and focused on the heat transfer using the numerical technique. Murtaza *et al.* [13,14] examined a fractal-fractional approach that was used to analyze the thermal performance of a nonlinear coupled stress ternary HNF in a channel. The Riga plates' performance in the presence of Ag and TiO_2 nanoparticles also affected the thermal field performance.

Chabani *et al.* [15] investigated the HNF flow through an enclosure with magnetohydrodynamics. The thermal investigation was highlighted in their research.

Ali *et al.* [16] studied the heat source and Lorentz force used to peristaltize the HNF through a micro-vessel. They focused on the drug delivery applications in the proposed model. Aich *et al.* [17] conducted a case study on HNF and magnetic nanofluid, which examined the effects of radiated hybrid nanoparticles on engine oil's thermal performance.

Mollah [18] found that the Riga plate affects the flow and heat transfer of HNFs through mixed convection. The HNF that occurred on a Riga plate in the presence of HNFs was analyzed by Senthilvadivu *et al.* [19]. The existence of the magnetic field improves the thermal performance of the HNFs. The presence of a magnetic field can improve the TC of the base fluid, as proposed by Dogonchi and Yasmin *et al.* [20].

The impact of this phenomenon is significant for various industrial applications, including electronic devices and heat exchangers. Panda *et al.* [21] examined an exponentially accelerated rotating porous surface used to transport the electromagnetohydrodynamic Casson HNF.

The thermal management system is influenced by viscous dissipation, which is another important feature of the energy equation. Viscous dissipation refers to the conversion of mechanical energy into thermal energy through internal friction. Energy transfer devices use this phenomenon extensively, and it plays a significant role in heat exchangers. The effect of viscous dissipation on thermal analysis and design of fluid-flow systems, including electronics cooling systems, microfluidic heat exchangers, and lubrication systems, was observed by Ihsan *et al.* [22]. Incorrect temperature distribution predictions, inefficient heat transfer, and compromised system performance can be a result of not considering viscous dissipation. Optimizing heat transfer processes and improving the efficiency and reliability of thermal management systems in various engineering applications require the appropriate incorporation of viscous dissipation phenomena. According to the cited literature, no investigation has been conducted to examine the fluid flow through a channel that has the Riga walls. Actually, in the context of converging and diverging Riga walls, the efficiency of nanoparticles contributes to improving the heat transfer more precisely. A gap exists in the current literature due to this issue. To address this gap, the current investigation aims to examine the converging and diverging channels that have the Riga walls, which more accurately reflect natural conditions. Thus, this study focuses on the more relevant phenomenon of Riga Walls to better understand the fluid dynamics in such channels. Moreover, in this work, blood is considered as the base fluid, while TiO_2 in combination with silver (Ag) are used as nanoparticles to get the HNF. The fluid flows through converging as well as diverging channels where the flow is induced by the convergent/divergent behavior of the Riga walls, such that the walls are stretchable/shrinkable. The governing partial differential equations (PDEs) are solved using the control volume finite element method (CVFEM) technique [23–25]. This method provides relevant information at a small level. The model equations have been changed to a dimensionless form using a set of appropriate variables and then evaluated by implementing the artificial neural network (ANN) approach [26–33].

1.1 Research questions

- How the HNF composed of Ag and TiO_2 enhances the heat transfer between converging and diverging Riga plates?
- Is the proposed problem compatible with the Riga walls due to the converging and diverging channels?
- What is the procedure for utilizing the CVFEM technique?
- Is it possible to test the validity of the problem?

1.2 Motivation

Utilization of Ag and TiO_2 HNF to test the thermal performance of the HNF is the main motive of this research. The non-parallel Riga walls have been used such that these walls converge and diverge, which have many applications. The direct PDE solution has been obtained using the CVFEM simulation, which predicts results at the micro-level and provides information about the HNF, especially regarding the increase in heat transfer. Using the ANN to solve the transformation equation is a new and advanced way to obtain outcomes.

In order to conduct future research, it is necessary to conduct a percentage analysis to calculate the enhancement in heat transfer.

1.3 Novelty

This study utilizes artificial intelligence (AI)-based computational intelligence approaches to analyze the dynamics of non-linear fluid problems. The following are the main highlights and novelty presented:

- Converging and diverging Riga plates benefit from the enhancement of heat transfer by the HNF composed of Ag and TiO_2. This particular model has a unique combination.
- The main contribution that has not been studied before is the Riga walls. The addition of Ag and TiO_2 also improves the newness of this model.
- The CVFEM is the primary method used to obtain the microscopic view of the fluid distribution. Heat transfer distribution and modified Hartman number (Ha) effect have wide applications. Researchers using the CVFEM approach have not previously studied this type of model.
- ANNs are combined to solve the new model problem in a novel way.

2 Problem formulation

In the formulation, two Riga plates are considered that are not parallel and have the ability to converge and diverge. The angle between these non-parallel Riga plates is assumed 2α. Riga wall stretching and shrinking are based on the radial direction depending on the nature of α. The extending and shrinking nature of the walls is denoted by the velocity $u = sr^{-1} = u_w$. In the proposed model, the velocity s stands for the rate of stretching and the velocity $u = u(r,\ \theta)$.

The surface temperature is denoted by T, such that $\alpha > 0$ is the divergent nature of Riga walls and $\alpha < 0$ stands for the convergence. In addition, the fundamental equations for the Ag and TiO_2 HNF are considered as follows [3,9,34,35]:

$$\rho_{\mathrm{hnf}}\left(\frac{u}{r} + \frac{\partial u}{\partial r}\right) = 0, \tag{1}$$

$$u\frac{\partial u}{\partial r} + \frac{1}{\rho_{\mathrm{hnf}}}\frac{\partial p}{\partial r} = \upsilon_{\mathrm{hnf}}\left(\frac{\partial^2 u}{\partial r^2} - \frac{u}{r^2} + \frac{1}{r^2}\frac{\partial^2 u}{\partial \theta^2} + \frac{1}{r}\frac{\partial u}{\partial r}\right) + \frac{J_0 B_0 d^2}{r^2}\mathrm{Exp}\left(-\frac{\pi}{a}\theta d\right), \tag{2}$$

$$\frac{r}{\mu_{\mathrm{hnf}}}\frac{\partial p}{\partial \theta} - 2\frac{\partial u}{\partial \theta} = 0, \tag{3}$$

$$\left(u\frac{\partial T}{\partial r}\right) = \frac{k_{\mathrm{hnf}}}{(\rho c_{\mathrm{p}})_{\mathrm{hnf}}}\left(\frac{\partial^2 T}{\partial r^2} + \frac{1}{r}\frac{\partial T}{\partial r} + \frac{1}{r^2}\frac{\partial^2 T}{\partial \theta^2}\right) + \frac{Q_0 T}{r^2(\rho c_{\mathrm{p}})_{\mathrm{hnf}}} + \frac{\mu_{\mathrm{hnf}}}{(\rho c_{\mathrm{p}})_{\mathrm{hnf}}}\left(\frac{1}{r^2}\left(\frac{\partial u}{\partial \theta}\right)^2 + 2\left(\frac{\partial u}{\partial r}\right)^2 + \frac{2u^2}{r^2}\right). \tag{4}$$

In the above equations, p is the pressure term in the momentum equations. The electric and magnetic field terms are denoted by J_0, B_0, respectively. The subscript hnf stands for the HNF, and f is used for the base solvent.

2.1 Thermophysical properties

The thermophysical description of Ag and TiO_2 HNFs can be found in the following equations:

$$\frac{\mu_{\mathrm{hnf}}}{\mu_{\mathrm{f}}} = \frac{1}{(1-\phi_{\mathrm{TiO_2}})^{2.5}(1-\phi_{\mathrm{Ag}})^{2.5}},$$
$$\frac{\rho_{\mathrm{hnf}}}{\rho_{\mathrm{f}}} = (1-\phi_{\mathrm{TiO_2}})\left\{(1-\phi_{\mathrm{Ag}}) + \phi_{\mathrm{Ag}}\frac{\rho_{\mathrm{Ag}}}{\rho_{\mathrm{f}}}\right\} + \phi_{\mathrm{TiO_2}}\frac{\rho_{\mathrm{TiO_2}}}{\rho_{\mathrm{f}}}, \tag{5}$$

$$\frac{k_{\text{hnf}}}{k_{\text{nf}}} = \left(\frac{k_{\text{TiO}_2} + 2k_{\text{nf}} - 2\phi_{\text{TiO}_2}(k_{\text{nf}} - k_{\text{TiO}_2})}{k_{\text{TiO}_2} + 2k_{\text{nf}} + \phi_{\text{TiO}_2}(k_{\text{nf}} - k_{\text{TiO}_2})} \right),$$
$$\frac{k_{\text{nf}}}{k_{\text{f}}} = \left(\frac{k_{\text{Ag}} + 2k_{\text{f}} - 2\phi_{\text{Ag}}(k_{\text{f}} - k_{\text{Ag}})}{k_{\text{Ag}} + 2k_{\text{f}} + \phi_{\text{Ag}}(k_{\text{f}} - k_{\text{Ag}})} \right), \tag{6}$$

$$\frac{(\rho C_{\text{p}})_{\text{hnf}}}{(\rho C_{\text{p}})_{\text{f}}} = (1 - \phi_{\text{TiO}_2}) \left\{ (1 - \phi_{\text{Ag}}) + \phi_{Ag} \frac{(\rho C_{\text{p}})_{\text{Ag}}}{(\rho C_{\text{p}})_{\text{f}}} \right\} + \phi_{\text{TiO}_2} \frac{(\rho C_{\text{p}})_{\text{TiO}_2}}{(\rho C_{\text{p}})_{\text{f}}}, \tag{7}$$

$$\frac{\sigma_{\text{hnf}}}{\sigma_{\text{nf}}} = \frac{(1 + 2\phi_{\text{TiO}_2})\sigma_{\text{TiO}_2} + (1 - 2\phi_{\text{TiO}_2})\sigma_{\text{nf}}}{(1 - \phi_{\text{TiO}_2})\sigma_{\text{TiO}_2} + (1 + \phi_{\text{TiO}_2})\sigma_{\text{nf}}},$$
$$\frac{\sigma_{\text{nf}}}{\sigma_{\text{f}}} = \frac{(1 + 2\phi_{\text{Ag}})\sigma_{\text{Ag}} + (1 - 2\phi_{\text{Ag}})\sigma_{\text{f}}}{(1 - \phi_{\text{Ag}})\sigma_{\text{Ag}} + (1 + \phi_{\text{Ag}})\sigma_{\text{f}}}. \tag{8}$$

2.2 Physical conditions

The initial and boundary conditions can be described through physical conditions as follows:

$$\left. \begin{aligned} u = \frac{u_c}{r}, \ \frac{\partial u}{\partial \theta} = 0, \ \frac{\partial T}{\partial \theta} = 0, \ \text{at } \theta \to 0, \ r \neq 0 \\ u = u_w = \frac{s}{r}, \ T = \frac{T_w}{r^2} \quad \text{as } \theta \to \pm\alpha. \end{aligned} \right\} \tag{9}$$

2.3 Similarity variables

This particular form is where the function is described as [3,9,34,35]

$$F(\theta) = ru(r, \ \theta). \tag{10}$$

The characteristics of non-dimensional transformations include

$$F(\eta) = \frac{F(\theta)}{u_c}, \ \Theta(\eta) = \frac{(Tr^2)}{T_w}, \ \eta = \frac{\theta}{\alpha}. \tag{11}$$

The transformed equations are based on equations (10) and (11).

$$(F''' + 4\alpha^2 F') + \frac{\mu_{\text{f}}}{\mu_{\text{hnf}}} \frac{\rho_{\text{hnf}}}{\rho_{\text{f}}} 2\alpha \ \text{Re} FF' + \frac{\mu_{\text{f}}}{\mu_{\text{hnf}}} (BHae^{-B\eta}) = 0, \tag{12}$$

$$\frac{k_{\text{hnf}}}{k_{\text{f}}} \text{Re}(\Theta'' + 4\alpha^2 \Theta) + \alpha^2 \left(\frac{(\rho c_{\text{p}})_{\text{hnf}}}{(\rho c_{\text{p}})_{\text{f}}} 2\text{Pr} \, \text{Re} F\Theta + \text{Re} \ Q\Theta \right) + \frac{\mu_{\text{hnf}}}{\mu_{\text{f}}} (4\alpha^2 \text{PrEc} F^2 + \text{PrEc}(F')^2) = 0. \tag{13}$$

Physical conditions that are simplified in the form of $F(\eta)$ and $\Theta(\eta)$ are expressed as follows:

$$\begin{aligned} &\Theta'(0) = C, \ \ \Theta(0) = C, \ \ F(0) = 1, \\ &F'(0) = 0, \ \ F(\pm 1) = \lambda, \ \ \Theta(\pm 1) = 1. \end{aligned} \tag{14}$$

The constant (C) stands as a constant of integration; $\lambda = \frac{s}{u_c} > 0, \lambda = \frac{s}{u_c} < 0$ stand for the stretching and shrinking, respectively. $\text{Pr} = \frac{(\mu C_{\text{p}})_{\text{f}}}{k_{\text{f}}}$ is the well-known Prandtl number; $\text{Ha} = \frac{J_0 B_0 \alpha^2 d^2}{u_c \mu_{\text{f}}}$ is the parameter obtained from the Riga walls known as the modified Ha. The dimensionless parameter $B = \frac{\pi a d}{a}$ is also obtained from Riga wall simplification. The other parameters of interest are Reynolds number $\text{Re} = \frac{r a u_c}{\upsilon_{\text{f}}}$ and Eckert number $\text{Ec} = \frac{u_c^2}{T_w (C_{\text{p}})_{\text{f}}}$. $u_w = \frac{s}{r}$ is the stretching and shrinking velocity depending on s. If ($s < 0$), it shrinks, if ($s > 0$), it then stretches. The motion at the central line is denoted by (u_{c}).

2.4 Heat transfer and skin friction

A specific rate is used to measure the heat transmission and drag force.

$$C_{\text{f}} = \frac{\mu_{\text{hnf}}}{\rho_{\text{hnf}} u_{\text{c}}^2} \left(\frac{1}{r} \frac{\partial u}{\partial \theta} \right) \Big|_{\theta = \pm\alpha},$$
$$\text{Nu} = \left(\frac{k_{\text{hnf}}}{k_{\text{f}}} \right) \left(\frac{\partial T}{\partial r} + \frac{1}{r} \frac{\partial T}{\partial \theta} \right) \Big|_{\theta = \pm\alpha}. \tag{15}$$

Equation (15) is included because of equations (9) and (10).

$$C_{\text{f}} = \frac{\mu_{\text{hnf}}}{\mu_{\text{f}}} \frac{1}{\text{Re}} |F'(\pm 1)|, \ \ \text{Nu} = \frac{k_{\text{hnf}}}{k_{\text{f}}} \frac{1}{r^2 \alpha} |\Theta'(\pm 1)|. \tag{16}$$

3 CVFEM solution

In porous and confined geometries where the fluid is moving, this method is typically utilized to resolve fluid flow issues. Various software tools are used to implement this method. The fluid flow between the two non-parallel Riga plates has been controlled using the FEA-Multiphysics software tool in the current scenario. The momentum and thermal equations in this software have been edited using our suggested model, which incorporates the physical conditions and thermophysical properties of nanomaterials mentioned in the problem. The governing equations are dealt with using the PDE form, and the transform equations are solved using the Morlet wavelet (MW) function.

3.1 Modeling with MW function

The MW formulation is defined as: $F(z) = \mathrm{Cos}(1.75z)e^{-0.5z^2}$.

The velocity and temperature fields are adjusted according to the transformed equations (12) and (13).

$$\begin{aligned}
\mathrm{Y}(z) &= \mathrm{Cos}(1.75z)e^{-0.5z^2}\\
\mathrm{Y}'(z) &= e^{-0.5z^2}\{-1.75z\sin(1.75z) - z\cos(1.75z)\},\\
\mathrm{Y}''(z) &= e^{-0.5z^2}\begin{Bmatrix}-3.14\cos(1.75z) + 1.8z\sin(1.75z)\\ -\cos(1.75z)+\\ 1.8z\sin(1.75z) + z^2\cos(1.75z)\end{Bmatrix}\\
\mathrm{Y}(z)''' &= e^{-0.5z^2}\begin{Bmatrix}3.0625z\cos(1.75z) + 4.43\sin(1.75z)\\ +1.64\sin(1.75z)\\ +3.0625ze^{-0.5z^2}\cos(1.75z)\\ -1.75z^2\sin(1.75z)\end{Bmatrix}.
\end{aligned} \tag{17}$$

Equation (17) is used to define the order of differential equations mentioned in equations (12) and (13). The MW performance for both equations (12) and (13) is further expanded as follows:

$$[F, \Theta] = \sum_{i=1}^{n} b_i \cos(1.75(J_i)) \times e^{-0.5(J_i)^2}, \tag{18}$$

$$\begin{aligned}
[F', \Theta'] = \sum_{i=1}^{k} b_i J_i (e^{-0.5(J_i)^2}\{&-1.75\sin(1.75(J_i))\\ &-(J_i)\cos(1.75(J_i))\}),
\end{aligned} \tag{19}$$

$$\begin{aligned}
&[F'', \Theta'']\\
&= \sum_{i=1}^{n} b_i J_i^2 \left\{e^{-0.5(J_i)^2}\begin{Bmatrix}-3.21\cos(1.75(J_i)) - \cos(1.75(J_i))\\ +1.7(J_i)\sin(1.75(J_i))\\ +(J_i)^2\cos(1.75(W_i)) + 1.7(J_i)\sin(1.75(J_i))\end{Bmatrix}\right\},
\end{aligned} \tag{20}$$

$$\begin{aligned}
&[F''']\\
&= \sum_{i=1}^{n} b_i J_i^2 \left\{e^{-0.5(J_i)^2}\begin{Bmatrix}5.359\sin(1.75(J_i)) + 3.06(J_i)\cos(1.75(J_i))\\ +1.75\sin(1.75(J_i)) - 1.75(J_i)^2\sin(1.75(J_i))\\ +3.06(J_i)\cos(1.75(J_i))\end{Bmatrix}\right\},
\end{aligned} \tag{21}$$

The expanded form of the solution obtained using $K_i = (J_i\eta + k_i)$ is expressed as follows:

$$F(\eta) = \begin{Bmatrix}(-2.6673)\cos(1.75(-0.16728\eta + 2.24516))\\ \times e^{-0.5(-0.1562\eta^* + 2.1452)^2}\\ +(2.421)\cos(1.75(-0.74352\eta + 1.68538))\\ \times e^{-0.5(-0.73829\eta + 1.6373)^2}\\ +(3.10234)\cos(1.75(0.34524\eta + 1.0644))\\ \times e^{-0.5(0.32562\eta + 1.26178)^2} + \cdots\end{Bmatrix}, \tag{22}$$

$$\Theta(\eta) = \begin{Bmatrix}(-0.99453)\cos(1.75(0.67373\eta + 0.271892))\\ \times e^{-0.5(0.4536\eta + 0.278192)^2}\\ +(1.2694)\cos(1.75(-1.5628\eta + 0.7830))\\ \times e^{-0.5(-1.25637\eta + 0.6289)^2}\\ +(0.3130)\cos(1.75(0.43673\eta + 0.56372))\\ \times e^{-0.5(-1.345\eta + 0.78453)^2} + \cdots\end{Bmatrix}. \tag{23}$$

4 Creating a formula for calculating fitness functions

$E = E_1 + E_2$ is a further expansion of the parts of mean squared error (MSE) function. $E = E_1 + E_2$ is used in the model equations.

$$\begin{aligned}
E_1 = \frac{1}{m}\sum_{i=1}^{m}\Bigg(&(F''' + 4\alpha^2 F')\\ &+ 2\alpha\frac{\mu_f}{\mu_{hnf}}\frac{\rho_{hnf}}{\rho_f}\mathrm{Re}\ FF' + \frac{\mu_f}{\mu_{hnf}}(BHae^{-B\eta})\Bigg)^2,
\end{aligned} \tag{24}$$

$$\begin{aligned}
E_2 = \frac{1}{m}\sum_{i=1}^{m}\Bigg(&\frac{k_{hnf}}{k_f}\frac{\rho c_{p\,f}}{\rho c_{p\,hnf}}(\mathrm{Re}\Theta'' + 4\,\mathrm{Re}\alpha^2) + \alpha^2\,\mathrm{Re}2\mathrm{Pr}F\Theta\\ &+ \frac{\mu_{hnf}}{\mu_f}\frac{\rho c_{p\ f}}{\rho c_{p\ hnf}}\mathrm{PrEc}((F')^2 + 4\alpha^2F^2)\Bigg)^2.
\end{aligned} \tag{25}$$

In the above equations, E is used for the MSE.

5 Discussion of results

The current study has taken into account the HNF made of Ag and TiO_2. The fluid flow is contemplated between the

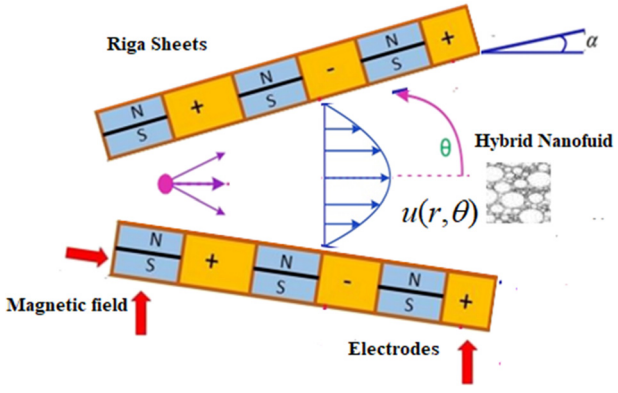

Figure 1: Geometry of the problem.

two Riga walls that come together and separate. The aim is to investigate the improvement in heat transfer. The base fluid is transformed into an HNF by dispersing Ag and TiO_2 solid nanoparticles. The thermal performance under converging and diverging conditions is the primary focus of this analysis based on the Riga wall concept. FEA-Multiphysics tools have been used to run the CVFEM. Editing model equations and adjusting the physical conditions are possible with this software based on the model problem.

5.1 ANN-hybrid cuckoo search (HCS)

AI is an advanced tool to predict the outputs of model problems using machine learning software that includes validation, prediction, and fitting functions. ANN is one of the key approaches to solving these types of problems. Additionally, ANN is divided into two parts: the backward data approach and the unsupervised approach. The current model problem is solved through the unsupervised method, that is ANN-HCS. The HCS results can be confirmed through updating the iterations of the method by using the fitness function in this scenario.

The results are displayed in figures and tables before being discussed.

Figure 1 illustrates the geometry of the problem that has the convergent and divergent Riga walls.

The simulation through the CVFEM provides a better understanding of the fluid flow in the converging and diverging channels. Predictions for the low and high fluid motions are provided by the contour and surface plots. Different flow scenarios are shown in Figure 2(a)–(d).

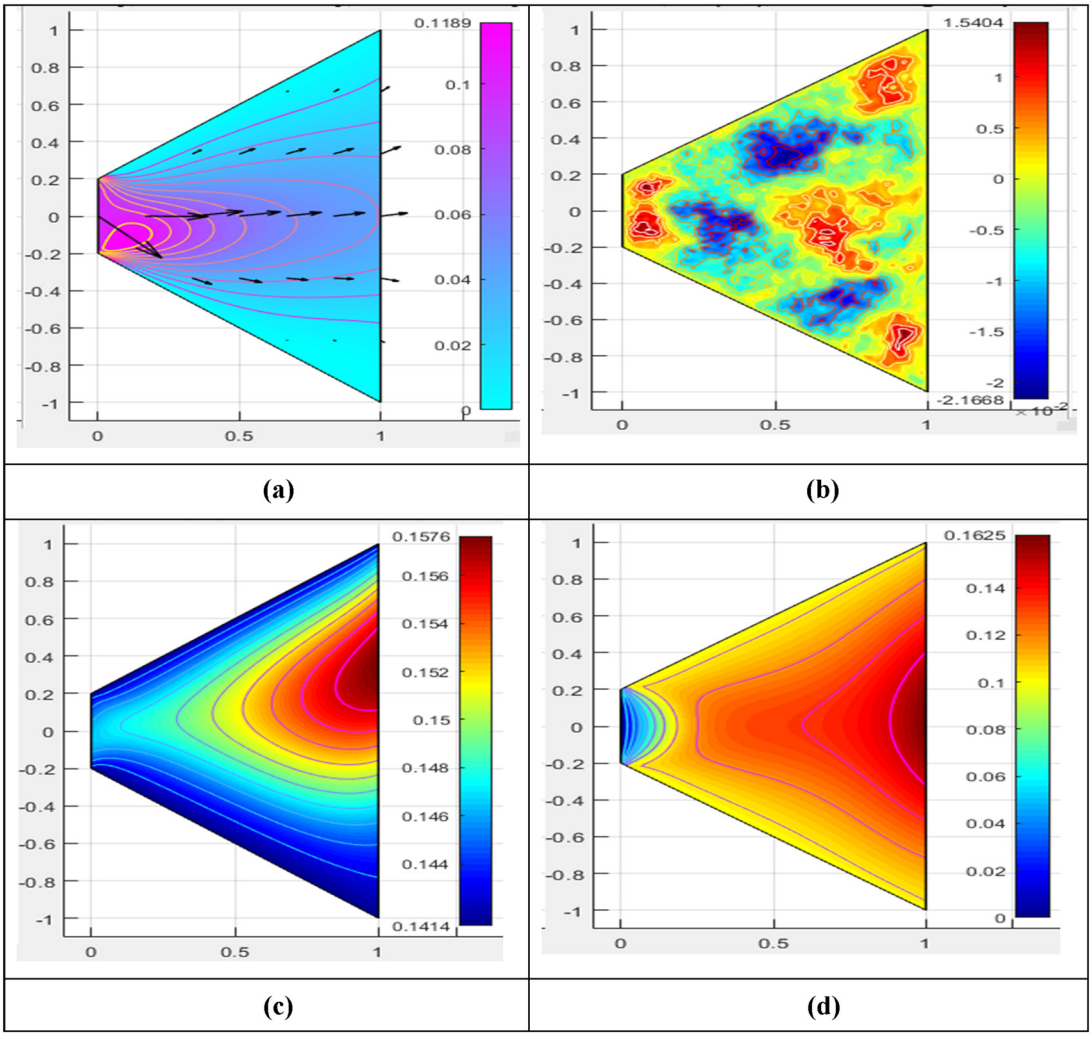

Figure 2: Velocity distribution, magnetic effect, temperature distribution, and fluid motion in various sections of the convergent and divergent channels. (a) Fluid flow in the channel. (b) Effect of magnetic potential. (c) Contour representation. (d) Fluid distribution in various sections.

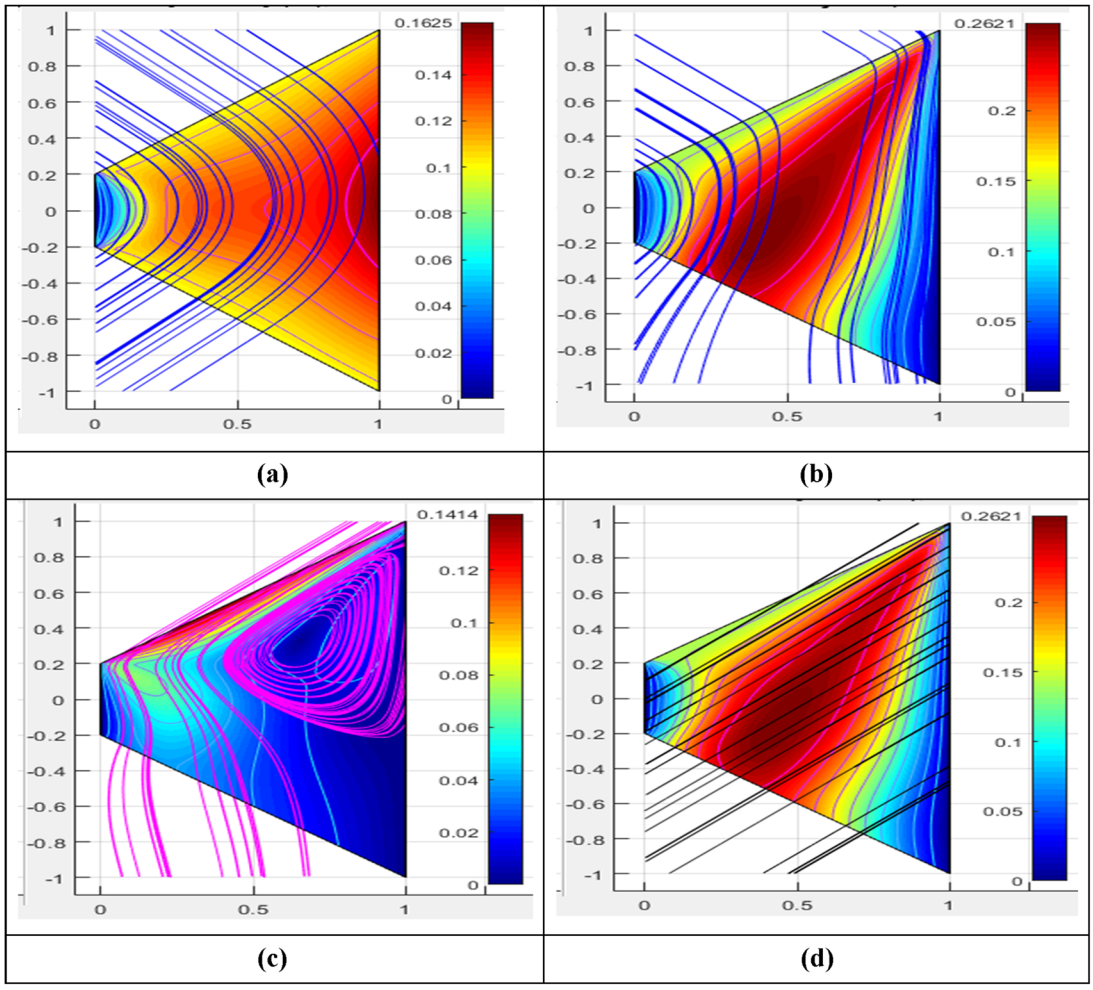

Figure 3: (a) Streamline scenario 1. (b) Streamline scenario 2. (c) Streamline scenario 3. (d) Streamline scenario 4.

These figures include the fluid motion and magnetic potential. The fluid flow's direction can be observed using the arrows in Figure 2(a). During the flow scenario, the effect of Riga walls is more significant in this proposed problem. In Figure 2(b), we can see the magnetic potential that disrupts the fluid motion. The fluid flow distribution can be predicted using the contour and surface plots, as demonstrated in Figure 2(c) and (d).

The tangential curve to the fluid motion is known as the streamlines. The streamlines provide the fluid flow pattern. These are very useful in the case of steady flow distribution to provide the accurate flow distribution. The uniform flow distribution and turbulence nature are shown in Figure 3(a)–(d). The streamline predicts the uniform flow distribution shown in Figure 3(a). Through the streamlines in Figure 3(b), the predictability of the turbulence near the Riga walls was established. As illustrated in Figure 3(c), the nature of turbulence becomes more apparent in the streamline scenario. The stream line in Figure 3(d) is characterized by the magnetic effect.

Different cases are shown in Figure 4 using the embedding parameters to show the ANN performance. The optimized method's optimization capabilities enable the HC algorithm to accomplish 30 distinct performances. In Case 1 to Case 4, the weight vectors show the performance of optimal outputs, as shown in Figure 4(a)–(d). Cases one through four are represented by the ideal mass vectors α_i, β_i, γ_i, $i = 1, 2, 3$ in Figure 4. These cases provide the error estimation for each optimal value.

Trial Case 1 to Case 4 for ENSE optimization are displayed in Figure 5(a)–(d). The use of fitness curves and fitness values is necessary to enhance neural networks for fluid dynamics study. These characters provide quantitative data that can be used to evaluate the precision of models in guessing the fluid motion and thermal profile. The growth of the neural network can be visualized using

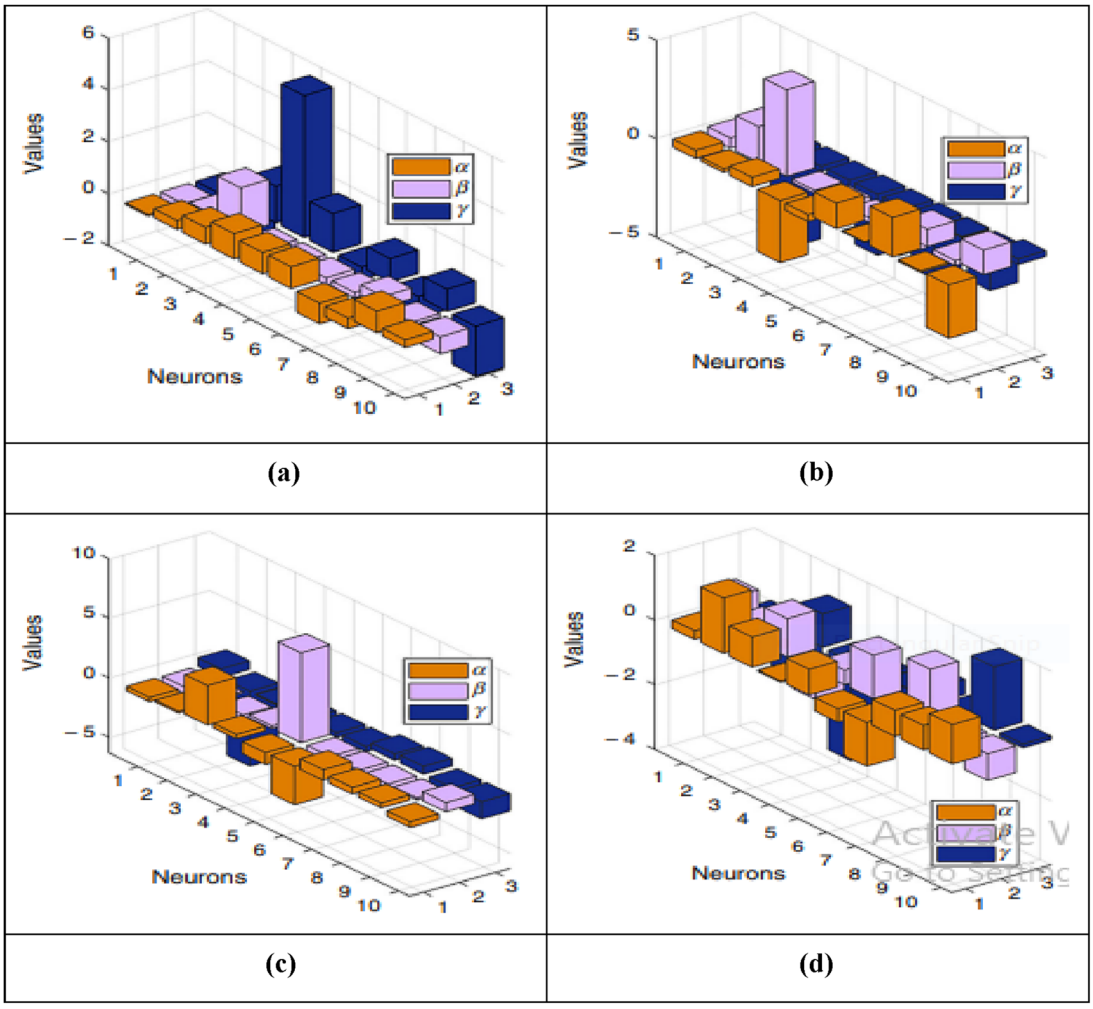

Figure 4: From Case 1 to Case 4, the best weight vectors from optimal outputs. (a) Case 1 weight vector from optimal outputs. (b) Case 2 weight vector from optimal outputs. (c) Case 3 weight vector from optimal outputs. (d) Case 4 weight vector from optimal outputs.

fitness functions that provide help to predict ENSE optimization. The collected findings are used to display the AE performance to identify similarities, as illustrated in Figure 5(a) for all cases starting from 2 to 5. The use of Ag and TiO_2 HNF can enhance heat transfer by avoiding complex data and delivering more meaningful results. The error estimation (AE) that has been obtained through trial for Case 1 lies in the range of 10^{-4} to 10^{-2}, as shown in Figure 5(a). In Case 2, this range lies from −0.01 to 0.015; in Case 3, the range is 10^{-3}; in Case 4, it is 10^{-3}, as shown in Figure 5(b)–(d), respectively. In Case 5, this range lies from −0.01 to 0.015, as shown in Figure 5(e). These results provide better heat transfer using the Ag and TiO_2 HNFs, avoiding the complex data. Optimizing embedded parameters during training is done by using the total information coefficient (TIC) in neural networks. This function has the capability to predict the accurate input data that is necessary for the training function and validating results. During the TIC training, redundant variables are automatically eliminated, and a prominent data sharing relationship is established.

Figure 6 displays the investigation of the most suitable values for TIC, which provide the accurate input variables. The TIC optimized value data range start from 10^{-4} and approach 10^{-2} for all possible cases. The TIC results shown in Figure 6(a) for Case 1 is in the 10^{-4} to 10^{-2} range. The range for the remaining Cases 25 are displayed in Figure 6(b)–(e).

In Case 2, this range lies from −0.01 to 0.015, for TIC optimization. In Case 3, the value is 10^{-3}; in Case 4, it is 10^{-3}, as shown in Figure 6(b)–(d) using TIC training, respectively. In Case 5, this range for TIC lies from −0.01 to 0.015, as shown in Figure 6(e). Using Ag and TiO_2 HNFs, these results provide better heat transfer, eliminating the need for complex data.

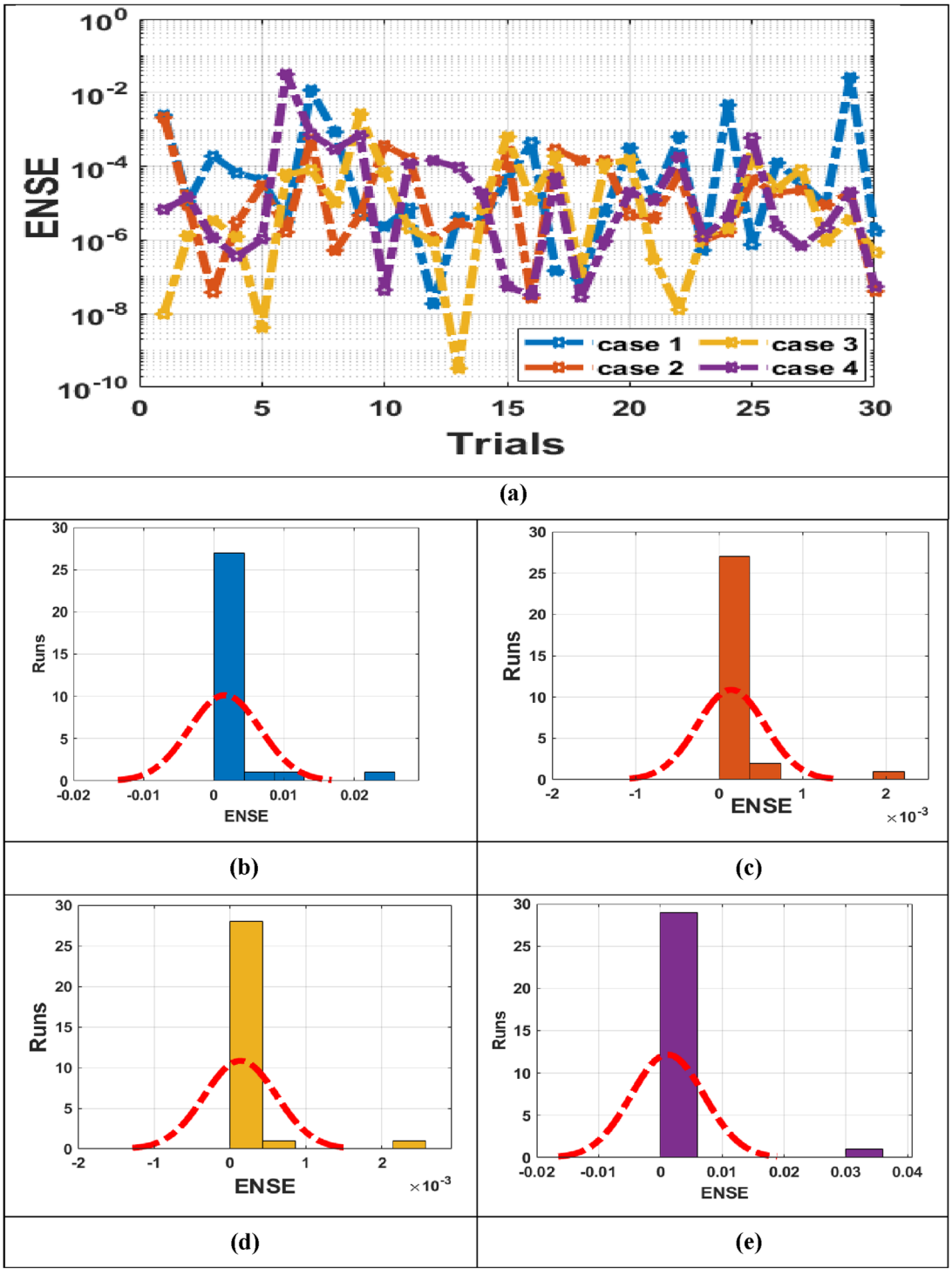

Figure 5: Case-1 to Case-5 were solved by utilizing statistical examples of trial-based error normalized squared error (ENSE) swarming strategies. (a) Trial Case 1 for ENSE optimization. (b) Trial Case 2 for ENSE optimization. (c) Trial Case 3 for ENSE optimization. (d) Trial Case 4 for ENSE optimization. (e) Trial Case 5 for ENSE optimization.

The fluid motion in terms of the convergent ($\alpha = -5°$) Riga walls is shown in Figure 7(a). The modified Ha increases, resulting in a decrease in the linear momentum of the Ag and TiO_2 HNF. The mobility of the fluid is reduced by nanosized particles, and fluid movement is hindered by resistance forces due to Ha effects. The Lorentz force is the resistance force that causes the fluid motion to decrease, which is the reason for the decline. The same scenario has

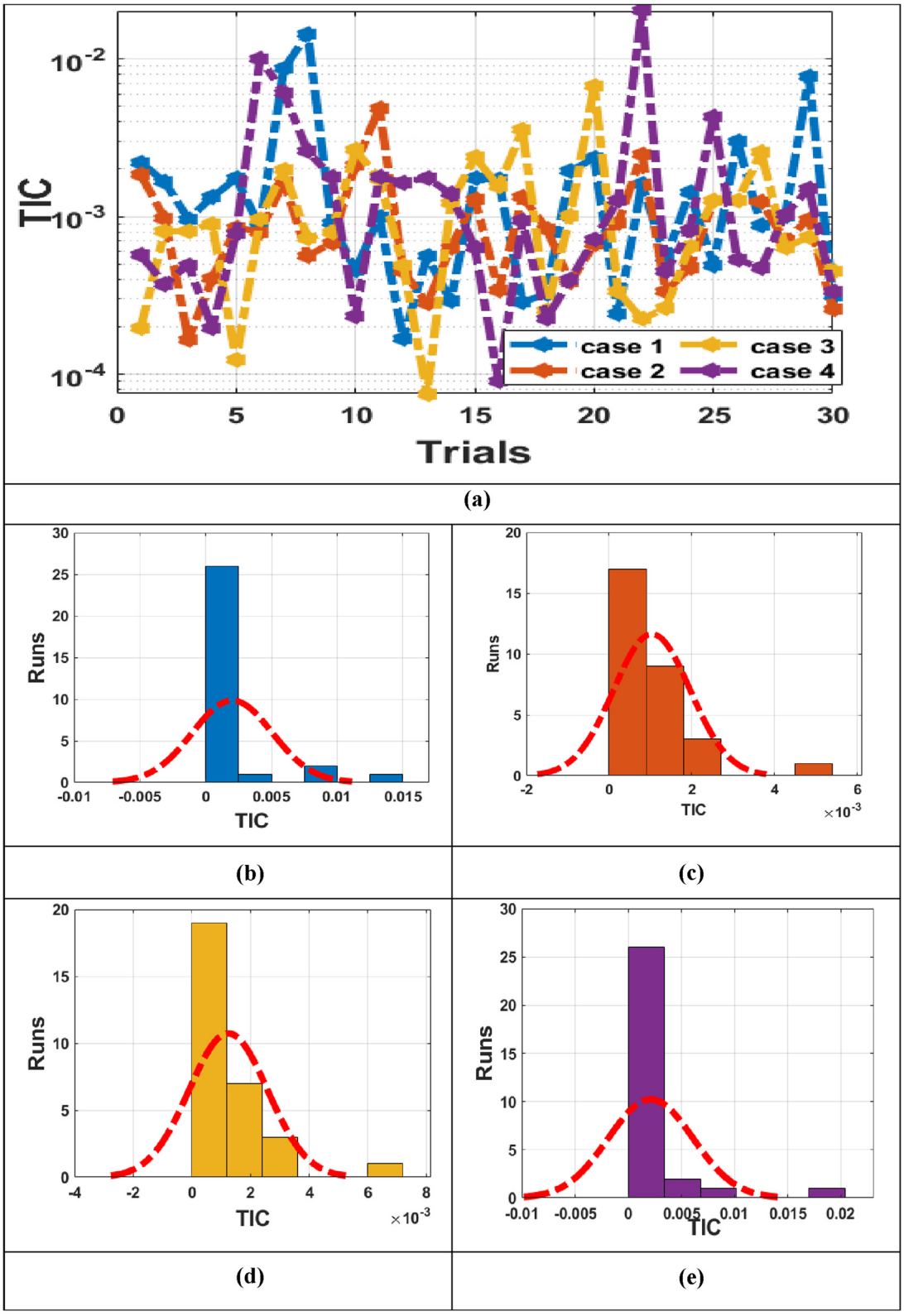

Figure 6: Case-1 to Case-5 were solved by utilizing statistical examples of trial-based TIC swarming strategies. (a) Trial Case 1 for TIC optimization. (b) Trial Case 2 for TIC optimization. (c) Trial Case 3 for TIC optimization. (d) Trial Case 4 for TIC optimization. (e) Trial Case 5 for TIC optimization.

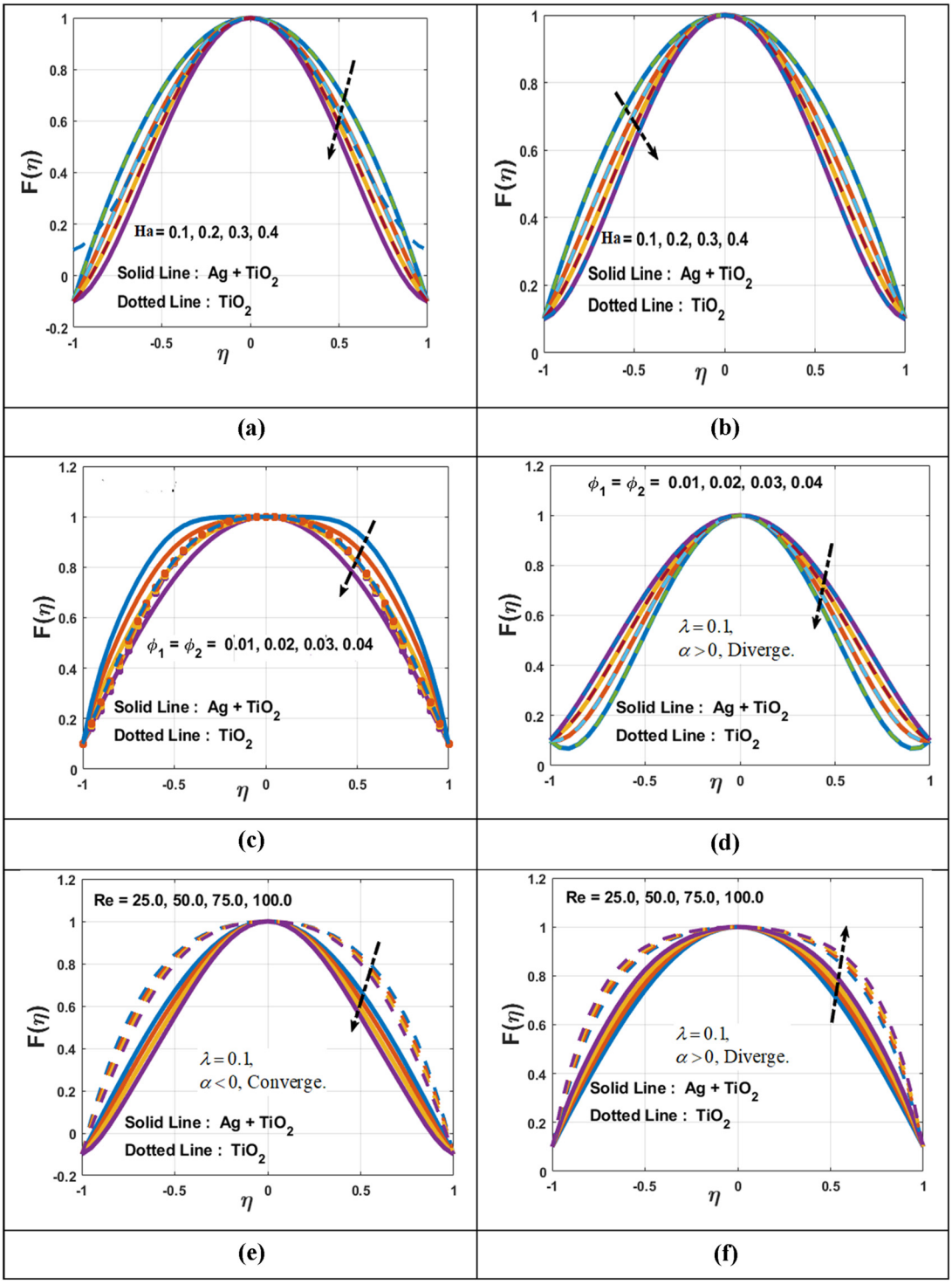

Figure 7: Impact of Ha, Re, $(\phi_1 + \phi_2)$ in the case of $\alpha = -5°$ and $\alpha = 5°$. (a) $F(\eta)$ *versus* Ha with $\alpha = -5°$. (b) $F(\eta)$ *versus* Ha with $\alpha = 5°$. (c) $F(\eta)$ *versus* $\phi_1 + \phi_2$ with $\alpha = -5°$. (d) $F(\eta)$ *versus* $\phi_1 + \phi_2$ with $\alpha = 5°$. (e) $F(\eta)$ *versus* Re with $\alpha = -5°$. (f) $F(\eta)$ *versus* Re with $\alpha = 5°$.

been shown for the divergent ($\alpha = 5°$) Riga walls, when increasing the values of Ha, as revealed in Figure 7(b).

Enhancing the thermal profile in both scenarios of the convergent and divergent Riga walls can be achieved by using the nanoparticle volume fraction $(\phi_1 + \phi_2)$ as an active candidate. However, in the case of fluid motion, the velocity field declines, as displayed in Figure 7(c) and (d). These results show that Ag and TiO_2 have the ability to

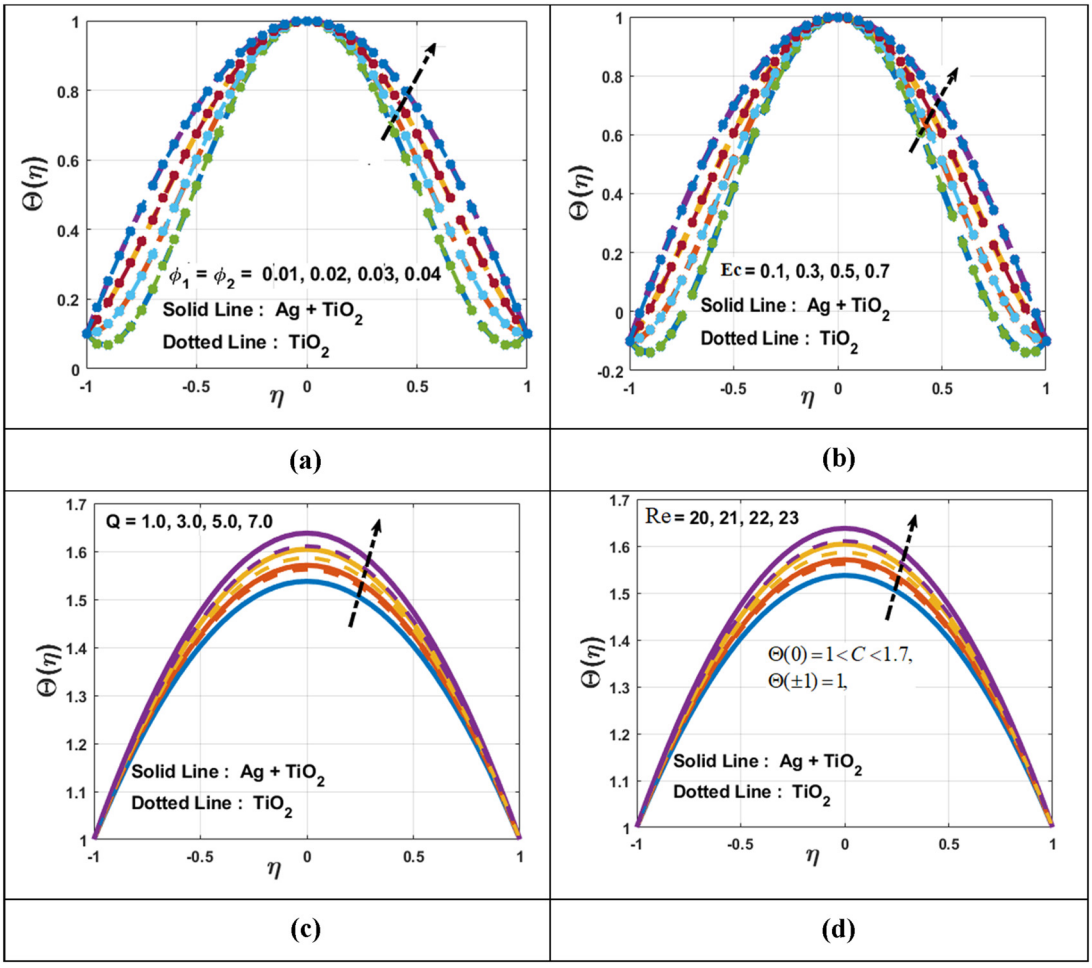

Figure 8: Impact of the thermal field $\Theta(\eta)$ on Ec, $(\phi_1 + \phi_2)$, Re, Q. (a) $\Theta(\eta)$ *versus* $\phi_1 + \phi_2$. (b) $\Theta(\eta)$ *versus* Ec. (c) $\Theta(\eta)$ *versus* Q. (d) $\Theta(\eta)$ *versus* Re.

Table 1: Thermophysical properties in numeric form

Materials	c_p (J/kg K)	ρ (kg/m^3)	k (W/m K)
TiO_2 (titanium dioxide)	686.2	4,250	8.954
Silver (Ag)	235	10,500	429

enhance the resistive force and decline the fluid motion. The high resistance force generated by the increasing Re can lead to a decrease in fluid motion, as shown for both cases in Figure 7(e) and (f). In the narrow channel, when there are higher inertial forces, the flow of fluid decreases. The resistance force of the walls of the Riga channel causes a decrease in flow velocity. When nanoparticles are included in the fluid, this decrease becomes more noticeable. In Figure 8, you can see the thermal profile $\Theta(\eta)$, which is the main focus of this research. Figure 8(a) illustrates the concentration of nanoparticles $(\phi_1 + \phi_2)$ that contribute to

Table 2: Case 1 utilizes the HNF-CC-TTBC model to determine the fluid's horizontal velocity

η	Mean	Min	Std	Max
0.1	2.6738×10^{-05}	2.672×10^{-08}	1.89322×10^{-06}	1.342×10^{-04}
0.3	2.67389×10^{-05}	4.89732×10^{-07}	3.98722×10^{-05}	3.67231×10^{-04}
0.5	6.67321×10^{-06}	2.9087×10^{-07}	1.98726×10^{-05}	1.8976×10^{-03}
0.7	3.8241×10^{-06}	1.9873×10^{-09}	4.9082×10^{-05}	3.89762×10^{-03}
0.9	6.8972×10^{-05}	4.89761×10^{-13}	356278×10^{-06}	2.7834×10^{-04}
1	1.90842×10^{-05}	2.89761×10^{-08}	4.6732×10^{-06}	3.9876×10^{-03}

Table 3: Case 1 utilizes the HNF-CC-TTBC model to determine the fluid's horizontal velocity

η	Min	Std	Mean	Max
0.1	4.45662×10^{-09}	2.765412×10^{-07}	3.908762×10^{-06}	3.627892×10^{-03}
0.3	3.7896×10^{-07}	$3.8976221 \times 10^{-05}$	$1.56425389 \times 10^{-05}$	2.987633×10^{-04}
0.5	2.56432×10^{-10}	$6.8765422 \times 10^{-05}$	4.786543×10^{-05}	9.085212×10^{-04}
0.7	2.5642×10^{-09}	$5.8976522 \times 10^{-05}$	$5.8976533 \times 10^{-06}$	3.0982×10^{-04}
0.9	1.9876×10^{-07}	$4.8976541 \times 10^{-06}$	$2.9876112 \times 10^{-05}$	1.786534×10^{-04}
1	3.78652×10^{-09}	$1.5642783 \times 10^{-07}$	1.895362×10^{-06}	$3.9876527 \times 10^{-04}$

Table 4: Validation of the results obtained through comparison

Re	$F''(\pm1)$, (Diverge) Ref. [34]	$F''(\pm1)$, (Diverge) Ref. [35]	$F''(\pm1)$, (Diverge) [Present]	$F''(\pm1)$, (Converge) Ref. [34]	$F''(\pm1)$, (Converge) Ref. [35]	$F''(\pm1)$, (Converge) [Present]
5	1.872807	1.872563	1.872578	0.9352672	0.9356738	0.9356732
7	1.934527	1.934782	1.934782	1.2671823	1.2674526	1.2674783
10	2.32672	2.3265627	2.326523	1.4526738	1.4525627	1.4525291

the enhancement of heat transfer $\Theta(\eta)$ by considering the convergent ($\alpha = -5°$) Riga walls. Enhancing the thermal profile and increasing the heat transfer rate are due to the high TC of the nanoparticle volume fraction ($\phi_1 + \phi_2$). The higher values of (Ec) increase heat transfer, resulting in a better thermal profile $\Theta(\eta)$, as depicted in Figure 8(b). Viscous dissipation using the Ag and TiO_2 nanoparticles is mostly compatible with the enhancement of the thermal field that happens with increasing values of (Ec). The thermal efficiency of the system is improved, and the movement of the Ag and TiO_2 particles is accelerated by the omission and absorption parameter (Q), as depicted in Figure 8(c). Efficient dissipation of excess energy is caused by the high absorption performance (Q), which contributes to stabilizing the energy profile $\Theta(\eta)$. The use of HNFs makes this effect more effective than the traditional fluid. The thermal profile $\Theta(\eta)$ increases as the (Re) value increases, as depicted in Figure 8(d). Exceeding the critical point results in a decrease in the thermal profile $\Theta(\eta)$ when the (Re) value is exceeded. Furthermore, the (Re) has an impact on the Nu by changing the heat transfer characteristics of the HNF. Convective heat transfer properties are modified by an increase in the (Re), which results in changes in decline to the thermal field.

The thermal and experimental characteristics of the nanomaterials are displayed in Table 1.

The use of statistical analysis in scientific investigations enables the compression, examination, and interpretation of data. Examining large datasets, confirming hypotheses, and drawing conclusions are possible by identifying patterns, trends, and links. The TIC (Threshold Linear Combination) function is used to handle nonlinearity in complicated data. Tables 2 and 3 present the TIC's best values in a range. Non-linearity in the ANN is

Table 5: Different parameters and skin friction relationship

ϕ	Ha	Re	$C_f(\alpha > 0)$, (TiO_2 + Ag)	$C_f(\alpha > 0)$, (TiO_2)	$C_f(\alpha < 0)$, (TiO_2 + Ag)	$C_f(\alpha < 0)$, (TiO_2)
0.02	**0.5**	**1**	**0.53672893**	**0.425642**	**1.452637**	**1.326172**
0.04			0.6178297	0.4261783	1.67893	1.4532672
0.05			0.72190232	0.5261782	1.728920	1.5267382
0.02	**0.5**	**1**	**0.53672893**	**0.425642**	**1.452637**	**1.326172**
	0.7		0.6278201	0.5362782	1.51637289	1.431782903
	0.9		0.8390212	0.6738921	1.62893022	1.52462734
0.02	**0.5**	**1**	**0.53672893**	**0.425642**	**1.452637**	**1.326172**
		5	0.67289132	0.53672831	1.6782910	1.52617822
		7	0.732891721	0.63728912	1.87392012	1.73829033

Table 6: Impact of different parameters on the Nusselt number Nu_x

Ec	Q	$Nu_x(\alpha > 0)$, Ag + TiO_2	$Nu_x(\alpha > 0)$, TiO_2	$Nu_x(\alpha < 0)$, Ag + TiO_2	$Nu_x(\alpha < 0)$, TiO_2
0.5	**0.5**	**8.8907832**	**8.5389078**	**12.2489313**	**11.3422489**
1		9.563782	9.3273563	13.0232350	12.2140232
2		10.1782903	9.7637829	14.1289363	13.5367228
0.5	**0.5**	**8.8907832**	**8.5389078**	**12.2489313**	**11.3422489**
	0.7	9.2617822	8.66738261	12.7890432	11.5367789
	0.9	9.7526819	9.0125268	13.236374	12.73822363

Table 7: Percentage increase in heat transmission rate when volumetric fraction values are increased

ϕ (%)	Nu_x, (TiO_2+Ag)	($\alpha > 0$)%	Nu_x, (TiO_2)	($\alpha > 0$)%	Nu_x, (TiO_2+Ag)	($\alpha < 0$)%	Nu_x, (TiO_2)	($\alpha > 0$)%
0	8.7692	0	8.7692	0	10.988	—	10.988	—
1	9.0132	2.707	8.9201	1.6	11.521	4.6	11.2892	2.6
2	10.008	12.3	9.1313	3.9	12.621	12.9	11.8672	7.4
3	10.86723	19.3	9.8921	11.3	13.78267	20.2	12.8425	14.4
4	11.02719	20.4	10.32782	15.09	14.6227	24.8	13.721	19.9
5	11.86273	26.1	10.89425	19.50	15.86273	30.7	14.52894	24.3

identified by the median absolute deviation (MAD) function, which is the main problem. In mathematical models, statistical analysis is used to predict the accuracy of the obtained results. The model's performance in different situations is also influenced by these trends, which determine its accuracy in fluid motion and temperature distribution. Informed decisions are made due to the extended limitations of the model problem.

To confirm the outputs, validation of the obtained results is necessary. Table 4 is used to compare the obtained results for this purpose. In this comparison, the common parameters are utilized, while the dissimilar parameters are not considered. The comparison shows that the present results closely match the previous literature [34,35] that validated the obtained results.

The skin friction is improved using the parameters ϕ, Re, Ha shown in Table 5. The HNF has shown a higher resistance rate than the TiO_2 nanofluids. This rate of increasing skin friction is the same for both the convergent and divergent Riga walls.

The improvement in the heat transfer rate is displayed in Table 6 utilizing the Ec and heat absorption parameter (Q). The improvement in the heat transfer rate is observed in both the convergent and divergent Riga walls. However, the improvement rate is comparatively higher in the case of convergent Riga walls. Also, HNFs consisting of Ag and TiO_2 are more prominent in improving the heat transfer rate.

The important results are displayed in Table 7, which shows an increase in the heat transfer rate using the nanoparticle volume fraction up to 5%. Initially, at 1% use of the nanoparticle concentration, the Nu increases from 9.0132 to 8.7692, showing an increase of 2.7% in the case of divergent Riga walls ($\alpha > 0$). Similarly, this increase in the heat transfer rate reaches 26.1% using the TiO_2 and Ag HNF, using a maximum of 5% use of ϕ when the Riga walls diverge. This increase is 1.6 and 19.5% for the 1 and 5% use of ϕ considering the TiO_2 nanofluid, which shows that the Ag and TiO_2 HNF is more efficient in the increase of the heat transfer rate.

The improvement in the heat transfer is prominent in the case when the Riga walls converge ($\alpha < 0$), as shown in Table 7. At first, the Nu increases from 10.988 to 11.21 when the nanoparticle concentration is 1%, indicating an increase of 4.6% when the convergent ($\alpha < 0$) Riga walls are involved, as shown in Table 7. When using the TiO_2 and Ag HNF, the heat transfer rate is 30.7% higher, and the maximum volume fraction is up to 5% when the Riga walls converge. The increase of 2.6 and 24.3% for 1 and 5% use of ϕ considering the TiO_2 nanofluid show that the Ag and TiO_2 HNF is more efficient in the increase of the heat transfer rate.

6 Conclusions

The flow of the Ag and TiO_2 HNF is examined using non-parallel Riga walls in this article. The goal is to enhance heat transfer by employing the HNF.

Two approaches are employed to solve the model problem. CVFEM techniques are used to solve the governing equations in the initial case. A wavelet-based physics-informed neural network solves the transformed equations during the second phase. The problem solution has been dealt with using the unsupervised ANN. The hybrid cuckoo algorithm can efficiently enhance solution performance by combining optimization and cuckoo search algorithms. By using an HCS algorithm, 30 different executions are selected to solve the model problem. By updating the method iterations, the fitness function is used by this scenario to confirm the HCS results.

These are the main findings of the current study:

1) The linear momentum of the Ag and TiO_2 hybrid nanoliquid decreases due to an increase in the Ha. The reason is that the magnetic effects cause resistance forces to hinder fluid movement.
2) The velocity of fluid flow declines with increasing values of ϕ in both cases of Riga walls.
3) A microscopic view of the particle distribution of HNFs can be obtained using the CVFEM technique. Specific information about the flow scenario is provided by the streamlines, surface plots, and contour plots.
4) It is observed that the heat transfer rate reaches 26.1% using the TiO_2 and Ag HNF, using a maximum of 5% use of ϕ when the Riga walls diverge. This increase is 1.6 and 19.5% for 1 and 5% use of ϕ considering the TiO_2 nanofluid, which shows that the Ag and TiO_2 HNF is more efficient in the increase of the heat transfer rate.
5) The improvement in the heat transfer is prominent in the case when the Riga walls converge ($\alpha < 0$). When using the TiO_2 and Ag HNF, the heat transfer rate is 30.7% higher, by using the maximum volume fraction up to 5%. This increase is 24.3% for 5% use of ϕ considering the TiO_2 nanofluid, which shows that the Ag and TiO_2 HNF is more efficient with the increase of the heat transfer rate.
6) The unsupervised technique of the ANN provides proper validation of the model problem in terms of the fitness fuzzy inference technique, MSE, ENSE, MAD, and TIC.

7 Future work

By incorporating the novel contribution that has been highlighted, the current work can be extended:

- The addition of different nanoparticles will make a significant contribution to adding three or more different nanoparticles to the same model.
- The current work is focused on the momentum and thermal boundary layers. A novel contribution can be made by adding the concentration equation.
- The double diffusion and motile microorganism concept will be a valuable addition.

Acknowledgments: The authors extend their appreciation to the Deanship of Research and Graduate Studies at King Khalid University for funding this work through the Large Research Project under grant number RGP2/463/46.

Funding information: This work was funded by the Deanship of Research and Graduate Studies at King Khalid University through the Large Research Project under grant number RGP2/463/46.

Author contributions: All authors have accepted responsibility for the entire content of this manuscript and approved its submission.

Conflict of interest: The authors state no conflict of interest.

Data availability statement: The datasets generated and/or analyzed during the current study are available from the corresponding author on reasonable request.

References

[1] Ahmed N, Abbasi A, Khan U, Mohyud-Din ST. Thermal radiation effects on flow of Jeffery fluid in converging and diverging stretchable channels. Neural Comput Appl. 2018;30:2371–9.
[2] Thumma T, Pyari DR, Ontela S. Optimizing heat transfer exploring the impact of exponential heat source on hybrid nanofluid in converging and diverging channels with sensitivity analysis. Mod Phys Lett B. 2025;39(23):2550065.
[3] Khan U, Adnan AN, Mohyud-Din ST, Baleanu D, Khan I, Nisar KS. A novel hybrid model for Cu–Al_2O_3/H_2O nanofluid flow and heat transfer in convergent/divergent channels. Energies. 2020;13(7):1686.
[4] Rehman S, Alqahtani S, Eldin SM, Hashim, Alshehery S. An extended model to assess Jeffery–Hamel blood flow through arteries with iron-oxide (Fe_2O_3) nanoparticles and melting effects: Entropy optimization analysis. Nanotechnol Rev. 2024;13(1):20230160.
[5] Yasir M, Khan M, Alqahtani AS, Malik MY. Heat generation/absorption effects in thermally radiative mixed convective flow of Zn-TiO_2/H_2O hybrid nanofluid. Case Stud Therm Eng. 2023;45:103000.
[6] Algehyne EA, Alamrani FM, Khan A, Khan KA, Lone SA, Saeed A. A comparative analysis of the blood-based hybrid nanofluid flow containing Cu and CuO nanoparticles over an exponentially extending surface. Proc Inst Mech Eng E: J Process Mech Eng. 2024;2024:09544089241235063.

[7] Kumar MN, Adnan, Ur Rahman K, Eldin MS, Bani-Fwaz ZM. Investigation of blood flow characteristics saturated by graphene/CuO hybrid nanoparticles under quadratic radiation using VIM: study for expanding/contracting channel. Sci Rep. 2023;13(1):8503.
[8] Bompally RKR, Gurijala R, Reddy RA, Thumma T. Effect of inclined magnetic field, non-uniform heat source on hybrid EG-MoS_2-SiO_2 radiative nanofluid flow with viscous and Joule dissipation over convectively heated elongating surface. Multiscale Multidiscip Model Exp Des. 2025;8(6):1–22.
[9] Alnahdi AS, Nasir S, Gul T. Ternary Casson hybrid nanofluids in convergent/divergent channel for the application of medication. Therm Sci. 2023;27(1):67–76.
[10] Li S, Li Y, Al Mesfer MK, Ali K, Jamshed W, Danish M, et al. Insights into the thermal characteristics and dynamics of stagnant blood conveying titanium oxide, alumina, and silver nanoparticles subject to Lorentz force and internal heating over a curved surface. Nanotechnol Rev. 2023;12(1):20230145.
[11] Jabir MS, Mohammed MK, Albukhaty S, Ahmed DS, Syed A, Elgorban AM, et al. Functionalized SWCNTs@Ag–TiO_2 nanocomposites induce ROS-mediated apoptosis and autophagy in liver cancer cells. Nanotechnol Rev. 2023;12(1):20230127.
[12] Kolsi L, Mir A, Muhammad T, Bilal M, Ahmad Z. Numerical simulation of heat and mass transfer through hybrid nanofluid flow consists of polymer/CNT matrix nanocomposites across parallel sheets. Alex Eng J. 2024;108:319–31.
[13] Murtaza S, Becheikh N, Rahman AU, Sambas A, Maatki C, Kolsi L, et al. Thermal performance analysis of a nonlinear couple stress ternary hybrid nanofluid in a channel: a fractal–fractional approach. Nanomaterials. 2024;14(22):1855.
[14] Murtaza S, Kumam P, Sutthibutpong T, Suttiarporn P, Srisurat T, Ahmad Z. Fractal-fractional analysis and numerical simulation for the heat transfer of ZnO + Al_2O_3 + TiO_2/DW based ternary hybrid nanofluid. ZAMM-J Appl Math Mech/Z Angew Math Mech. 2024;104(2):e202300459.
[15] Chabani I, Mebarek-Oudina F, Ismail AAI. MHD flow of a hybrid nano-fluid in a triangular enclosure with zigzags and an elliptic obstacle. Micromachines. 2022;13(2):224.
[16] Ali A, Mebarek-Oudina F, Barman A, Das S, Ismail AI. Peristaltic transportation of hybrid nano-blood through a ciliated micro-vessel subject to heat source and Lorentz force. J Therm Anal Calorim. 2023;148(14):7059–83.
[17] Aich W, Khan SU, Ishaq M, Fateh MO, Ghachem K, Ayadi B, et al. Applications of radiated tri-hybrid nanoparticles (TiO_2-CuO-SiO_2) on the thermal performance of engine oil (SA E10W-30): A case study on HNF and MNF. Case Stud Therm Eng. 2025;70:106144.
[18] Mollah MT. EMHD laminar flow of Bingham fluid between two parallel Riga plates. Int J Heat Technol. 2019;37(2):641–8.
[19] Senthilvadivu K, Eswaramoorthi S, Loganathan K, Abbas M. Time-dependent Darcy–Forchheimer flow of Casson hybrid nanofluid comprising the CNTs through a Riga plate with nonlinear thermal radiation and viscous dissipation. Nanotechnol Rev. 2024;13(1):20230202.
[20] Yasmin H, Hejazi HA, Lone SA, Raizah Z, Saeed A. Time-independent three-dimensional flow of a water-based hybrid nanofluid past a Riga plate with slips and convective conditions: A homotopic solution. Nanotechnol Rev. 2023;12(1):20230183.
[21] Panda S, Shamshuddin MD, Pattnaik PK, Mishra SR, Shah Z, Alshehri MH, et al. Ferromagnetic effect on Casson nanofluid flow and transport phenomena across a bi-directional Riga sensor device: Darcy–Forchheimer model. Nanotechnol Rev. 2024;13(1):20240021.
[22] Ihsan A, Ali A, Khan AU. Thermal analysis of electroosmotic flow in a vertical ciliated tube with viscous dissipation and heat source effects: implications for endoscopic applications. J Therm Anal Calorim. 2024;150:2727–41.
[23] Alqarni MM, Alghamdi S, Ullah MZ, Aljohani MA, Gul T, Mahmoud EE. The flow of hybrid nanofluids between nonparallel stretching walls using neural network and control volume finite element method. Int J Numer Methods Heat Fluid Flow. 2025;35(7):2484–508.
[24] Khan A, Aljuaydi F, Khan Z, Islam S. Numerical analysis of thermophoretic particle deposition on 3D Casson nanofluid: Artificial neural networks-based Levenberg–Marquardt algorithm. Open Phys. 2024;22(1):20230181.
[25] Alderremy AA, Sulaiman M, Ullah MZ, Abualnaja KM, Alghamdi W, Gul T, et al. Utilization of a micro-squeezed channel in drug delivery through hybrid nanofluids under Hall current, nanoparticle radius, and interparticle spacing effects. Int J Numer Methods Heat Fluid Flow. 2025;35(5):1764–89.
[26] Assiri TA, Gul T, Khan Z, Muhammad T, Alhabeeb SA, Ali I. Artificial neural networks strategy to analyze the magnetohydrodynamics Casson-Maxwell nanofluid flow through the cone and disc system space. Int J Heat Fluid Flow. 2024;107:109406.
[27] Habib S, Nasir S, Khan Z, Berrouk AS, Islam S, Aamir A. Modeling of chemically reactive fluid dynamics with thermal effect and energy source through a magnetized medium. J Therm Anal Calorim. 2025;150:4631–51.
[28] Alnahdi AS, Khan A, Gul T, Ahmad H. Stagnation point nanofluid flow in a variable darcy space subject to thermal convection using artificial neural network technique. Arab J Sci Eng. 2024;49:11309–26.
[29] Gul T, Alharbi SO, Khan I, Khan MS, Alzahrani S. Comparative analysis of the flow of the hybrid nanofluid stagnation point on the slippery surface by the CVFEM approach. Alex Eng J. 2023;76:629–39.
[30] Algehyne EA, Raizah Z, Gul T, Saeed A, Eldin SM, Galal AM. Cu and Al_2O_3-based hybrid nanofluid flow through a porous cavity. Nanotechnol Rev. 2023;12(1):20220526.
[31] Islam N, Akhtar Y, Ahmad S, Junjua MUD, Hendy AS, Alballa T, et al. Advancing drug delivery: Neural network perspectives on nanoparticle-mediated treatments for cancerous tissues. Nanotechnol Rev. 2024;13(1):20240129.
[32] Zhang X, Zhang P, Wang T, Zheng Y, Qiu L, Sun S. Compressive strength and anti-chloride ion penetration assessment of geopolymer mortar merging PVA fiber and nano-SiO_2 using RBF–BP composite neural network. Nanotechnol Rev. 2022;11(1):1181–92.
[33] Shoaib M, Ali F, Awais M, Naz I, Shamim R, Nisar KS, et al. Intelligent computing for the double-diffusive peristaltic rheology of magneto couple stress nanomaterials. Nanotechnol Rev. 2023;12(1):20220557.
[34] Ahmad S, Farooq M. Double-diffusive Hamel–Jeffrey flow of nanofluid in a convergent/divergent permeable medium under zero mass flux. Sci Rep. 2023;13(1):1102.
[35] Zada L, Ullah I, Nawaz R, Jamshed W, Saddam EN, Idris SA, et al. Computational treatment and thermic case study of entropy resulting from nanofluid flow of convergent/divergent channel by applying the lorentz force. Case Stud Therm Eng. 2024;54:104034.